ORIGINAL ARTICLE

Evaluation of interfacial heat transfer coefficient based on the experiment and numerical simulation in the air-cooling process

Liping Zou[1] · Lidan Ning[1] · Xiaowei Wang[2] · Zhichao Li[1,3] · Lianfang He[1] · Huiping LI[1]

Abstract

Air-cooling process is a very complex heat transfer involving the heat transfer theory and the fluid dynamics. In the paper, the experiment and numerical simulation methods are used to study the interfacial heat transfer and gas flow in the process of air-cooling, and an axisymmetric model is established to simulate the air-cooling process based on the fluid-thermal-solid coupling method. In the experiment and numerical simulation, the high-speed compressed air is used to impinge and cool the hot metallic surface. The temperatures attained in the experiment and numerical simulation are used to calculate the interfacial heat transfer coefficient (IHTC) by a self-developed inverse heat transfer analysis software. Considering the influence of turbulence model on flow, it found that the SST $k-\omega$ turbulence model is more appropriate for the air-cooling process. Based on the SST $k-\omega$ model, the effect of sample diameter and jet distance (distance from jet to cooling surface) on the flow pattern and temperature fields is studied, the results show that the temperatures attained in the numerical simulation are in good agreement with those of experiment, and the smaller the jet distance is, the bigger the IHTC is. Finally, the IHTCs under the different jet distance and inlet flow velocity are calculated based on the temperature curves attained in the numerical simulation.

List of symbols

T	Temperature (°C)
ρ	Density (kg·m^{-3})
C_p	Specific heat (J·kg^{-1}·°C^{-1})
λ	Thermal conductivity (W·m^{-1}·°C^{-1})
t	Time (s)
Z	Direction in cylindrical coordinate system (m)
r	Direction in cylindrical coordinate system (m)
q	Surface heat flux (W·m^{-2})
T_f	Temperature of compressed air (°C)
τ	Total shear stress (Pa)
τ_l	Shear stress due to the laminar flow (Pa)
τ_T	Shear stress due to the wall turbulence (Pa)
u	Flow velocity (m·s^{-1})
v	Kinematic viscosity (m^2·s^{-1})
ε_m	Turbulent momentum diffusivity (m^2·s^{-1})
q_T	Heat flux in wall turbulence (W·m^{-2})
q_r	Heat flux contributed by wall turbulence (W·m^{-2})
α	Laminar thermal diffusivity (m^2·s^{-1})
ε_T	Turbulent thermal diffusivity (m^2·s^{-1})
μ_T	Turbulent viscosity (m^2·s^{-1})
u_i	Flow velocity (m·s^{-1})
μ	Dynamic viscosity (m^2·s^{-1})
k	Turbulence Kinetic Energy (m^3·s^{-2})
ω	Turbulent Dissipation Rate (m^2·s^{-3})
H	Jet distance (m)
d	Diameter of sample(m)
Nu	Nusselt number
G_k	Generation of k
G_ω	Generation of ω
Γ_k	Effective diffusivity of k
Γ_ω	Effective diffusivity of ω
Y_k	Dissipation of k
Y_ω	Dissipation of ω
D_ω	Generation of ω

✉ Huiping LI
lihuiping99@163.com

1 School of Materials Science and Engineering, Shandong University of Science and Technology, 579 Qianwangang Road, Qingdao, Shandong 266510, PR China

2 School of Materials Science and Engineering, Shandong University, 17923 Jingshi Road, Jinan, Shandong 250061, PR China

3 Shandong Province Key Laboratory of Mine Mechanical Engineering, Shandong University of Science and Technology, Qingdao 266590, China

1 Introduction

In the air-cooling quenching, the compressed air impinges upon the sample surface through a nozzle at a high speed to achieve the forced convection heat transfer. Air-cooling quenching is widely used in the cooling of the extruded and rolled aluminum alloy [1], nickel-based powder high-temperature alloy [2], heavy rail [3], stainless steel [4] and so on. Compared with the traditional quenching process, air-cooling quenching has many advantages, such as an easily-controlled cooling rate, a lower thermal stress and quenching distortion in the sample, an easily-controlled interfacial heat transfer coefficient (IHTC) and pollution-free.

The IHTC refers to the heat transfer coefficient between the sample surface and the quenchant, which includes the radiation and convective heat transfer coefficients. The IHTC is generally used as the third boundary condition to calculate the temperature field of sample in the numerical simulation of hot working process, such as quenching [5–7], metal hot forming [8, 9] and other processes with heat conduction [10–12]. In the air-cooling process, there are many factors which can significantly affect the cooling rate, phase transformation, quenching distortion, hardness and residual stress of quenched parts, and the IHTC is one of the factors which can be easy to control and has the greatest effect on the quenched parts. The IHTC directly affects the distribution of temperature field, and then affects the subsequent calculation of phase transformation and distortion of sample. Accurate IHTC is beneficial to improve the credibility of the simulation results. Therefore, studying the influence of process parameters on the IHTC can provide theoretical basis and guidance for the design and optimization of air cooling process.

The IHTC can not be directly tested by experiment, it can only be evaluated according to the temperature curves attained in the experiment or numerical simulation by the the inverse heat transfer method based on finite difference method [9], controlled volume method [13], finite element method (FEM) [5, 7] and other methods. The evaluation of IHTC is one of the inverse heat conduction problems (IHCP), it is an ill-posed problem and more difficult to solve than the direct heat conduction problem (DHCP). In the evaluation of IHTC, the temperature is usually measured directly with sensors placed beneath the cooling surface, and the temperature corresponding to the position of sensors is estimated in the solution of IHCP. The relationship between the surface temperature and IHTC can be attained by the iterative calculation and the comparison of temperature difference between the experiment and the solution of IHCP [5, 14]. But the experiment of air-cooling process is complicated, and the temperatures measured in the experiment are affected by the accuracy of the instrument and other factors. With the popularity of large-scale commercial numerical simulation software, the multi-physics coupling analysis can be carried out to obtain the temperature of sample in the air-cooling process.

The fluid–solid coupled analysis of heat transfer in the air-cooling process is worthy of attention, some scholars have simulated the temperature and velocity field, and optimized the parameters of air-cooling process. Yang et al. [15] simulated the air-cooling process of heavy rail, the flow field of air jet nozzle and the temperature field of heavy rail in air cooling process were obtained, it provides some reference data for the adjustment of jet cooling parameters in the air cooling process. Yang et al. [16] simulated the transient conjugate heat transfer of the cryo-supersonic air-quenching of a metal disk, and the result shown that the decline rate of stagnation temperature gradually increases with the increase of the inlet pressure. Xu et al. [1] simulated the distribution of temperature and stress of aluminum alloy in the process of online air cooling, and the results showed that the strain of aluminum alloy in the air-cooling process is small. Xu et al. [17] installed an air-cooling system on the ball screw pair, and established a finite element model to simulate the temperature distribution, thermal deformation and air-cooling performance, in order to overcome the thermal error and achieve temperature balance more quickly. In the above mentioned references, the research work only gave the numerical simulation of the temperature or flow velocity, but the IHTC was not calculated.

For the samples with simple shapes and small sizes, the multi-physics coupling analysis can be carried out using Fluent software, and the temperature, stress and distortion of the parts in the cooling process can be obtained. However, for parts with complex shapes and big sizes, it is difficult to conduct the multi-physics coupling analysis. In order to attain the reliable IHTC and ensure the accuracy of numerical simulation for the complex parts in the air-cooling process by regarding the cooling surface as the third boundary condition, the effect of flow velocity and jet distance (distance from jet to cooling surface) on the IHTC is studied in the paper by means of experiment, numerical simulation and the inverse heat transfer method, and a relatively accurate model which can simulate the velocity field of air-cooling process is determined. Based on the temperature curves attained by experiment and the multi-physics coupling analysis, the IHTCs in the air-cooling process are evaluated by the inverse heat transfer method.

2 Experimental facilities and procedure

2.1 Experimental facilities

The material used in the experiment is 304 stainless steel. The size of the sample is Ø10 mm × 30 mm, the
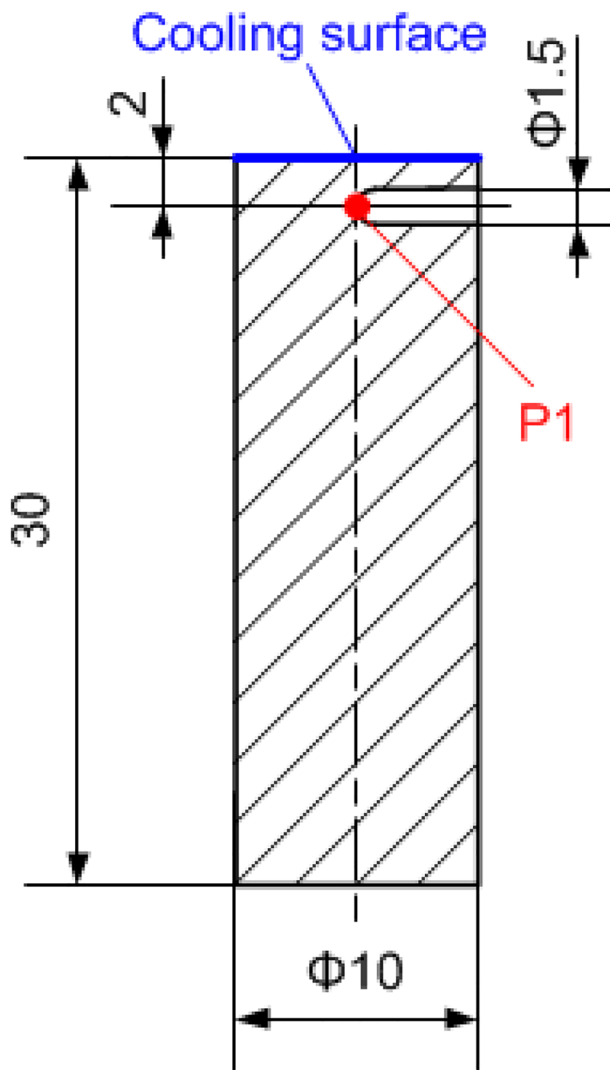
Fig. 1 Sample size

diameter of the hole which is used to insert the thermocouple is 1.5 mm, the distance from center line of the hole to the cooling surface is 2 mm, as shown in Fig. 1. The chemical composition is shown in Table 1. The density is

7930 kg·m^{-3}, and other thermo-physical parameters are shown in Table 2.

The microstructure of 304 stainless steel is austenite, there is no phase transformation in the heating and cooling process, so the latent heat of phase transformation can not be considered in the numerical simulation. As shown in Fig. 2, the surrounding and bottom surfaces of the sample are wrapped by the aluminum silicate ceramic fiber. During the experiment, the sample is placed in the induction coil with an inner diameter of 50 mm, and the thermocouple is inserted into the temperature measuring hole as shown in Fig. 2.

The experimental devices of air-cooling mainly include an induction heating device (water circulating system, induction heating power and electrical control cabinet), an air compressor, a gas pressure regulating valve on the prefilter, a flowmeter, a temperature data acquisition system (K-type thermocouple, temperature recorder and data acquisition software PicoLog), as shown in Fig. 3. The power supply is IGBT digital intelligent intermediate frequency induction power supply. The flowmeter model CMF5008A has an accuracy of 1.5%FS and a response time of 20 ms. The air compressor used in the experiment has a capacity of 100 L and a nominal flow of 300 L•min^{-1}. The maximum rate of A/D converter for high-speed temperature data acquisition equipment (USB TC-08) is 10 cycles per second. The K-type armored thermocouple with a diameter of 1.5 mm has a measurement error of ± 1.0 °C and a response time of 0.02 s in the temperature range from 0 °C to 1200 °C.

2.2 Experimental procedure

In the experiment, an IGBT digital control of induction heating power supply is used to heat the sample to 800 °C, and the compressed air is used to cool the end surface of the sample, the heating and cooling process are shown as Fig. 4. This heating method shown in Fig. 4 can make the sample have an uniform temperature along the radical and axial directions [19]. The pressure regulating value controls the pressure of flow, the flux is measured by the flowmeter, and

Table 1 Chemical composition of 304 stainless steel

Composition	Cr	Ni	Mn	Si	C	P	S
wt%	18.2%	8.35%	1.92%	0.97%	0.07%	0.043%	0.025%

Table 2 Thermal conductivity and specific heat of 304 stainless steel [18]

Temperature, °C	20	100	200	300	400	500	600	700	800	900	1000
Thermal conductivity W·m^{-1}.°C^{-1}	15.9	16.3	18	18.8	20.1	21.4	23.9	25.5	26.8	26.8	28.1
specific heat J·Kg^{-1}.°C^{-1}	511	511	528	544	565	590	-	628	641	645	649

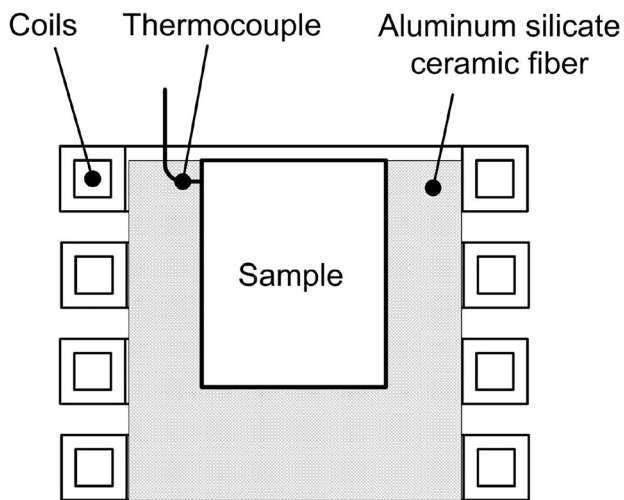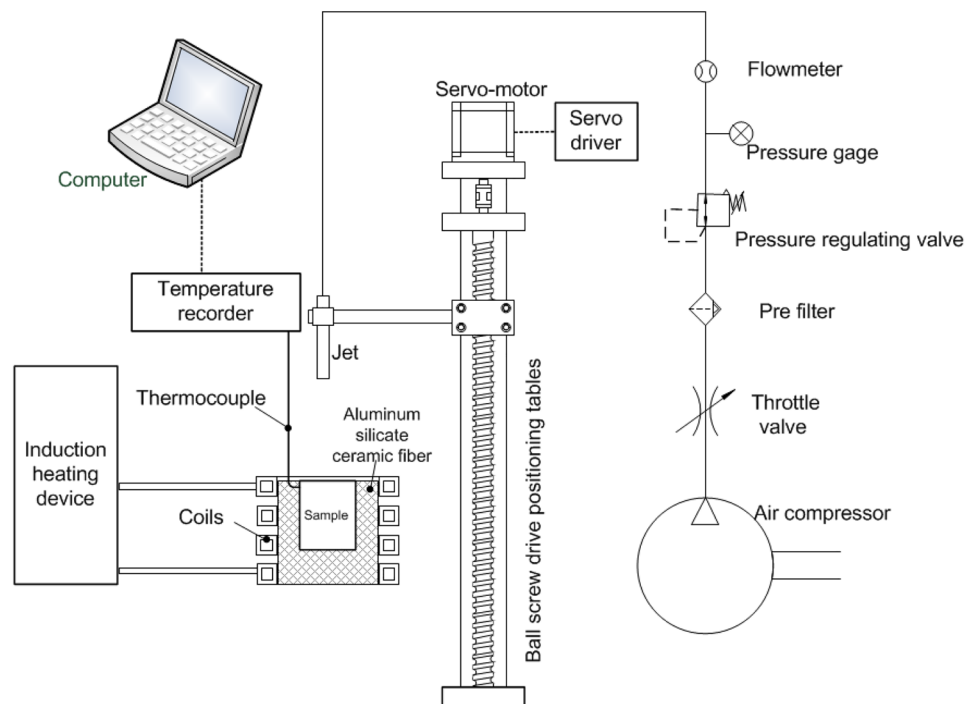Coils   Thermocouple   Aluminum silicate
ceramic fiber

Fig. 2 Sample with aluminum silicate ceramic fiber installed in induction coil

the flow rate can be calculated by the flux. The jet distance is adjusted by the ball screw drive system which is controlled by servo driver. K-type thermocouple, temperature recorder and data acquisition software (PicoLog) are used to monitor the heating and cooling curves of the sample at the position P1 (as shown in Fig. 1), the time interval of sampling is 400 ms. The gas pressure is 0.2 MPa. The flux is 253.6 L/min, the diameter of the nozzle is 6.5 mm, the flow velocity is 127.4 m/s.
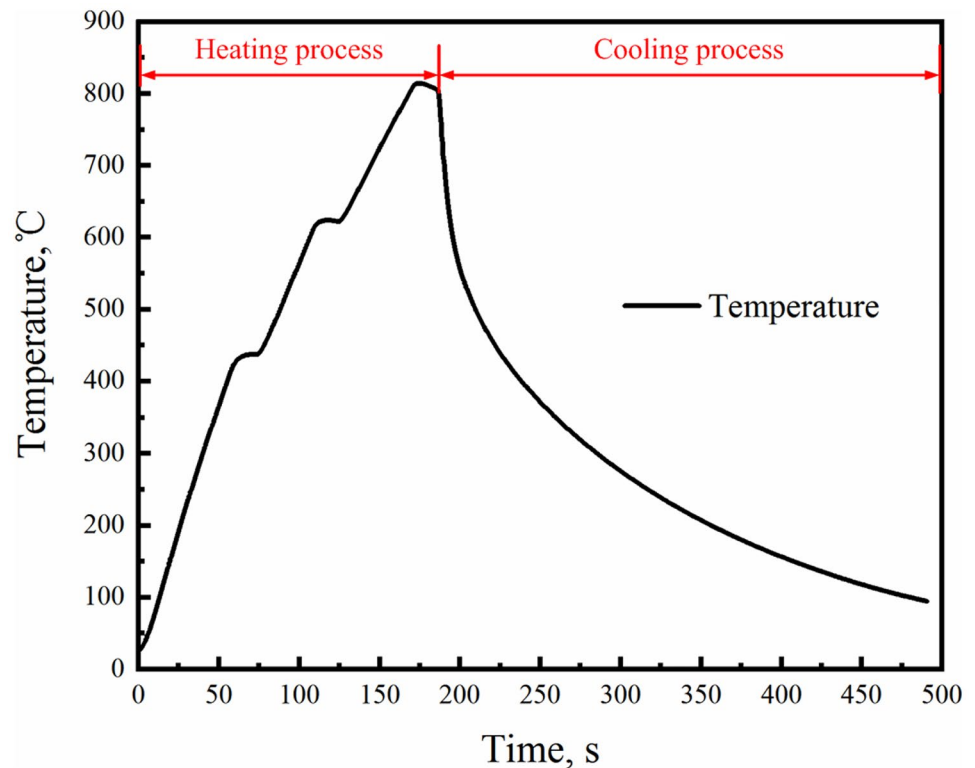
3 Inverse heat transfer analysis

The solution of IHTC is an IHTP. It is an ill-posed problem and more difficult to solve than the normal heat exchange problem. For IHTP, if the temperature is known, and some thermal-physical parameters or initial conditions are unknown, the unknown parameters can be calculated by FEM and other algorithms based on the temperature field. According to the temperature curves measured in the experiment and attained in the numerical simulation, the surface temperature, interfacial heat transfer coefficient and surface heat flux are solved by a self-developing inverse heat transfer program based on the improved advance and retreat method and golden section method (GSM) [5, 7]. The Fortran program of the improved advance and retreat method is shown in Appendix 1, and the Fortran program of GSM is shown in Appendix 2.

3.1 Criteria of convergence

According to the characteristic of evaluating the IHTCs in the air-cooling process, the criterion of convergence is described using temperature T attained by thermocouple and the temperature $\hat{T}$ evaluated by inverse heat transfer analysis.

$$Error = T - T \tag{1}$$

$$Error = T^{(t)} - \hat{T}_i^{(t)} \tag{2}$$

Fig. 3 Diagram of experimental device

Fig. 4 Heating and cooling process

where, $f = |Error| \leqslant \delta$ is the difference between temperature T attained by thermocouple and the temperature $\hat{T}$ evaluated by inverse heat transfer analysis. f is the absolute value of error. δ is a very small number. $T^{(t)}$ is the temperature measured at time t. $\hat{T}_i^{(t)}$ is the temperature of ith iteration at time t by the numerical simulation. If f is not more than δ, the IHTCs at time t can be attained.

3.2 Finding an interval by advance-retreat method

The advance-retreat method can be used to finding the minimum or maximum of an unimodal function. The principle of this method can be described as follows: Search an interval from an initial point (temperature) along one direction, until find three points (temperatures) which make the absolute value of error in Eq. (1) showing "up-down-up" trend; If it is not successful along this direction, then retreat the starting point and search the interval along other direction (along an inverse direction), as shown in Fig. 5

In the process of finding an interval by the advance-retreat method, two end-points of the interval is regarded as the value of IHTC and used to evaluate the temperatures in the numerical simulation. The IHTC relative to the left end-point of objective interval will make the value of Eq. (1) being positive (more than 0), and the IHTC relative to the right end-point of objective interval will make the value of Eq. (1) being negative (less than 0).

There are several iterations at time t. The values of $\hat{T}_i^{(t)}$ will vary with the IHTC in each iteration, and the error values relative to the different IHTC can be calculated by Eq. (1) and (2). There is only one appropriate IHTC, which will let the error being enough small, and this IHTC is the objective to be found.

The interval size depends on the step size of finding an interval by the advance-retreat method. If the step size is bigger, the iteration numbers in the process of reducing the interval size by gold section method (GSM) will be increased largely. If the step size is smaller, the iteration numbers of finding an interval by the advance-retreat method will be increased largely. In order to decrease the iteration numbers of finding an interval, the step size in the advance-retreat method is a variable. The flow chart of improved advance-retreat method is shown in Fig. 6.

3.3 Calculation of IHTC by GSM

GSM is a method for finding the minimum or maximum of an unimodal function by successively narrowing the interval size. In the calculation of IHTC by GSM, the function values relative to the different probe points are compared to narrow the interval in which the optimum value is included, and the approximative value of the function extremum will be achieved when the interval size is reduced to a prescriptive value.

Fig. 5 Schematic diagram of advance-retreat method [14]
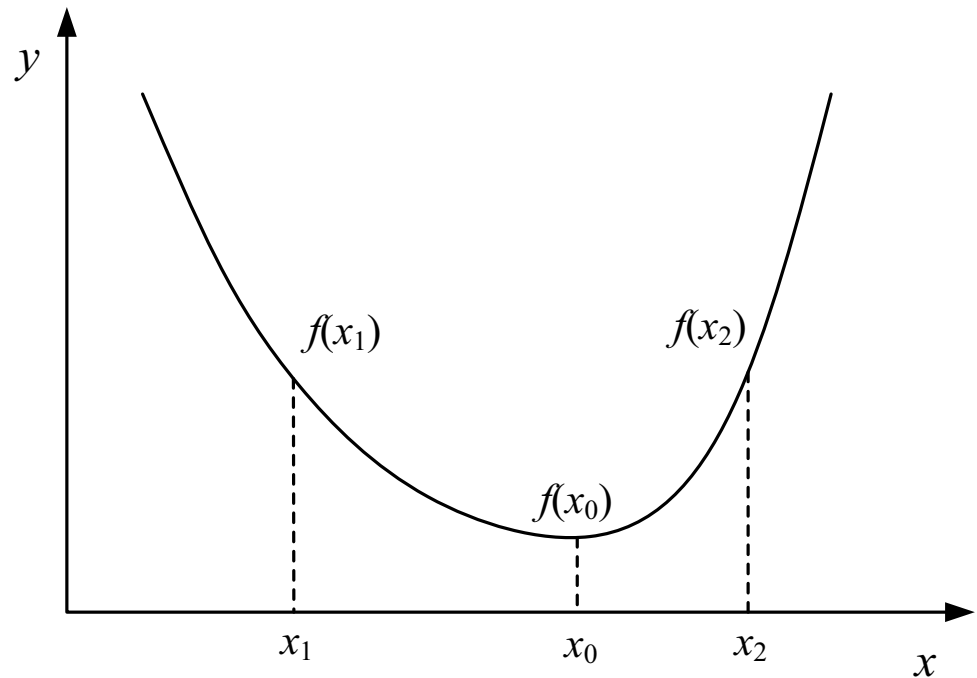
As shown in Fig. 7, the error values are the y—axis, and the IHTCs are the x-axis. The values of error at the two end-points of interval a, b have already been evaluated by the improved advance-retreat method show in Fig. 6. Since $E(a)$ is more than 0, and $E(b)$ is less than 0, it is clear that there is a value of IHTC which can minimize the functional values of $E(x)$ in the interval a, b. The process of narrowing the interval size by GSM is shown in Fig. 8.

3.4 FEM model of evaluating the IHTC

According to the temperature curves measured in the experiment and attained in the numerical simulation, the IHTCs are calculated by the inverse heat transfer method. The FEM mesh and boundary conditions are shown in Fig. 9. The lower end surface and the cylinder surface are set as the adiabatic boundary $h_0 = 0$, and the upper end surface is the cooling surface between the sample and flow, h_1 is the IHTC calculated by the inverse heat transfer method.

The heat conduction equation of sample shown in Fig. 9 can be described as

$$\rho C_p \frac{\partial T}{\partial t} = \frac{1}{r}\frac{\partial}{\partial r}(r\lambda\frac{\partial T}{\partial r}) + \frac{\partial}{\partial z}(\lambda\frac{\partial T}{\partial z}) \tag{3}$$

where T is temperature (°C), ρ is density ($kg \cdot m^{-3}$), C_p is capacity ($J \cdot kg^{-1} \cdot °C^{-1}$), λ is thermal conductivity ($W \cdot m^{-1} \cdot °C^{-1}$), t is time (s), z and r are the direction in cylindrical coordinate system.

During the experiment, the surrounding and bottom surfaces of the sample are wrapped by the aluminum silicate

ceramic fiber with an extremely low thermal conductivity (0.026–0.035 W·m^{-1}·°C^{-1} [20]), according to the definition of heat transfer coefficient and thermal conductivity, the heat transfer coefficient is approximately equal to the ratio of thermal conductivity to thickness of the material. The thickness of thermal insulation material around sample is 20 mm, then the heat transfer coefficient between sample and atmosphere is approximately 1.3–1.75 W·m^{-2}·°C^{-1}, so the heat transfer at the bottom surface and around the cylinder can be ignored, and it can be assumed to be a one-dimensional heat transfer process. The one-dimensional heat conduction equation can be described as

$$\rho C_p \frac{\partial T}{\partial t} = \frac{\partial}{\partial z}(\lambda\frac{\partial T}{\partial z}) \tag{4}$$

The initial conditions:

$$T|_{t=0} = f(z) \tag{5}$$

The boundary conditions:

$$\frac{\partial T}{\partial z}|_{h_0} = 0 \tag{6}$$

$$-\lambda\frac{\partial T}{\partial z}|_{h_1} = h_1(T - T_f) \tag{7}$$

Tf is the temperature of compressed air.

The flow chart of the inverse heat transfer program is shown in Fig. 10.

The calculation accuracy of heat transfer coefficient is of great significance for the other simulation. With the
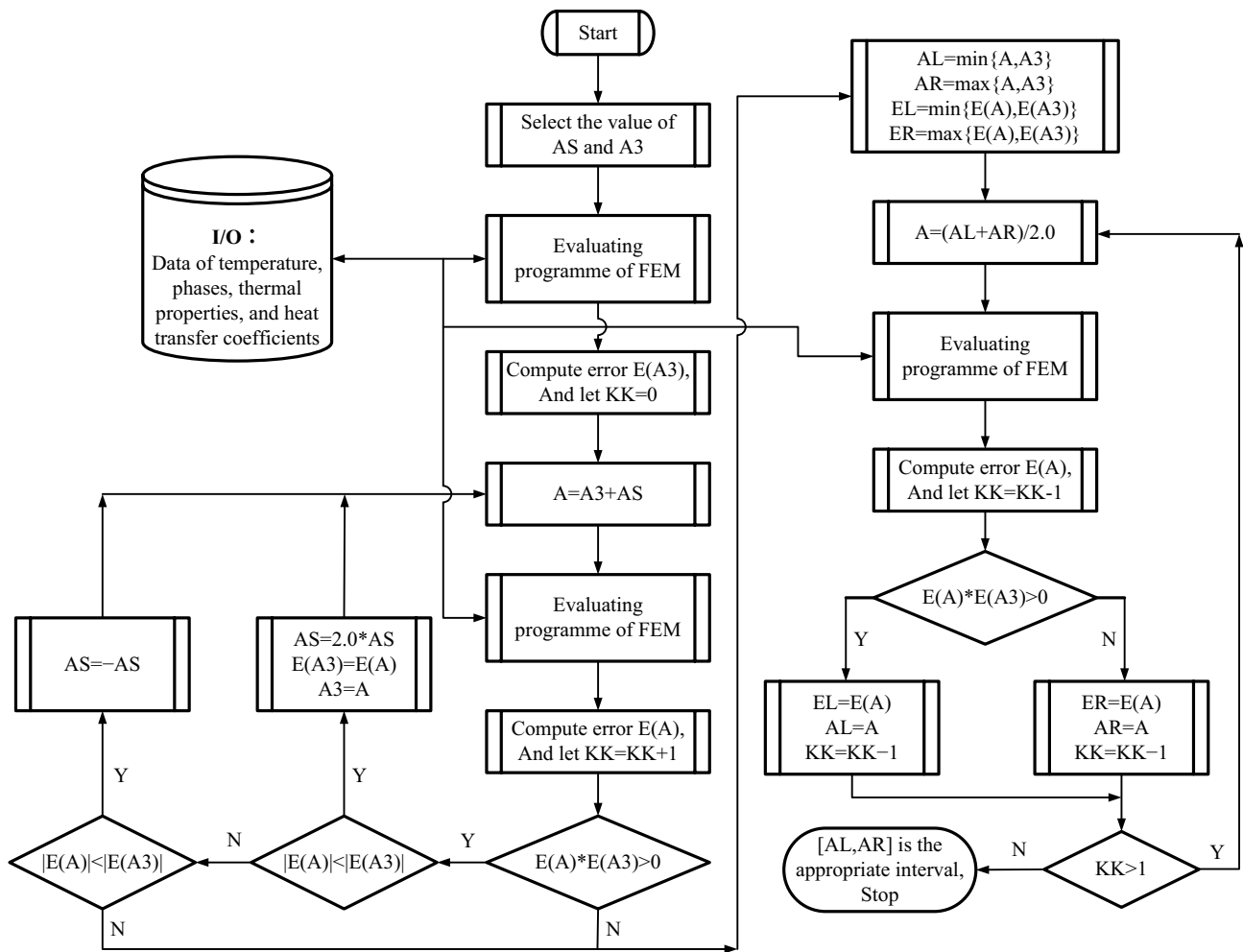
Fig. 6 Flow chart of improved advance-retreat method [14] (AL is the left end-point of interval, AR is the right end-point of interval, AS is the step size, A3 is the initial value, E(A) and E(A3) are the errors cal-culated by Eq. (1), min{ }and max{ } are the function of finding the minimum and maximum of error)

development of inverse heat transfer research, the calculation accuracy of inverse heat transfer is gradually improved with

Fig. 7 Schematic diagram of GSM [14]

the application of different algorithms. The error between the algorithm used in this paper and the temperature measured by experimental thermocouple is shown in Fig. 11, and the accuracy of the error is up to 0.0001, and the maximum error is not more than 0.004. It is believed that the calculation result is reliable.
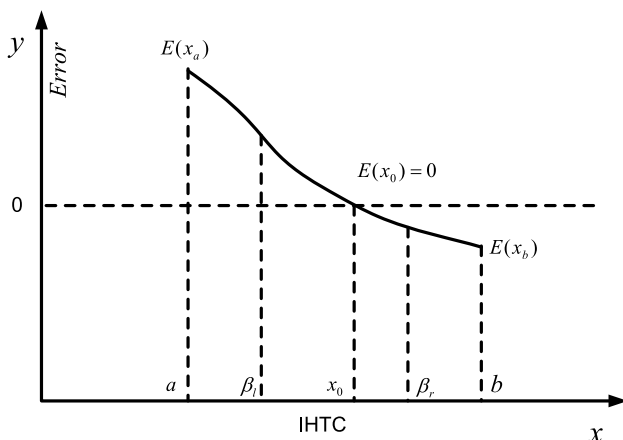
4 Simulation

4.1 Turbulence model

In the present problem, the SST k-ω model is adapted. The transport equations for turbulent kinetic energy (k) and turbulent dissipation rate (ω) are as follows:

$$\frac{\partial}{\partial t}(\rho k) + \frac{\partial}{\partial z_i}\left(\rho k u_i\right) = \frac{\partial}{\partial z_j}\left(\Gamma_k \frac{\partial k}{\partial z_j}\right) + G_k - Y_k \tag{8}$$
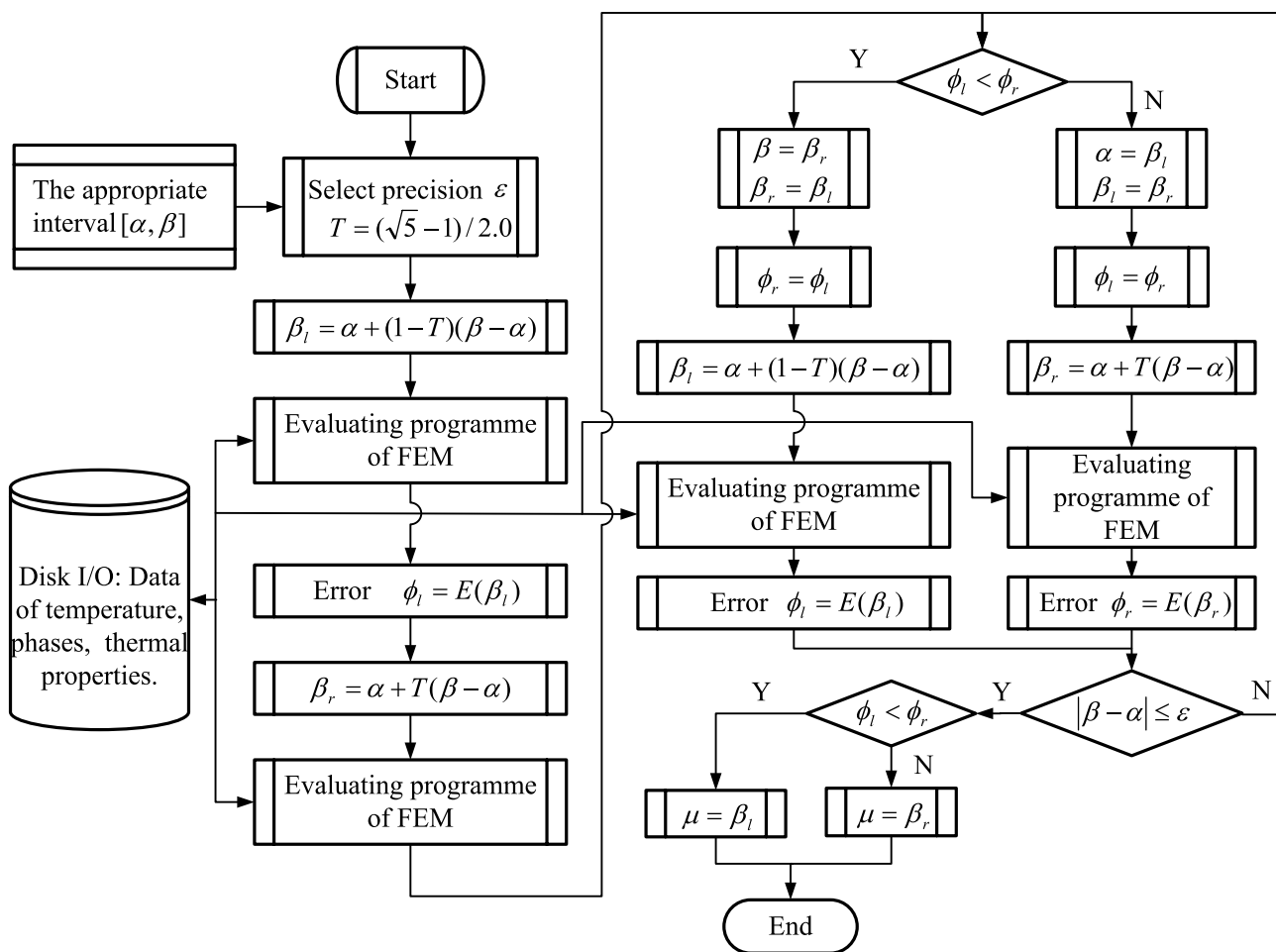
Fig. 8 Process of narrowing the interval size by GSM 14 (α and β are the two end-points of interval attained by the improved advance-retreat method, μ is the IHTC attained by GSM β_l is the left probe point of interval, β_r is the right probe point of interval, τ is the solu-tion of quadratic equation $\tau^2 + \tau - 1 = 0$, φ_l and φ_r relative to the left and right probe points are calculated using Eq. (2) according to the temperature attained in the numerical simulation)

$$\frac{\partial}{\partial t}(\rho\omega) + \frac{\partial}{\partial z_i}(\rho\omega u_i) = \frac{\partial}{\partial z_j}\left(\Gamma_\omega \frac{\partial \omega}{\partial z_j}\right) + G_\omega - Y_\omega + D_\omega \quad (9)$$

In the SST k-ω model, ρ represents density, u_i represents mean velocity, z_i and z_j represent the directions of turbulence, G_k represents the generation of turbulence kinetic energy due to mean velocity gradients. G_ω represents the generation of ω. Γ_k and Γ_ω represent the effective diffusivity of k and ω, respectively. Y_k and Y_ω represent the dissipation of k and ω due to turbulence. D_ω represents the other generation of ω The detailed analysis can be found in the Fluent Guide.

4.2 Geometry and boundary conditions

To simulate the gas flow pattern and temperature of the sample, the model is established to consider the fluid region and solid region, as shown in Fig. 12. The quadrilateral grids are used to mesh the fluid region and solid region to achieve the better convergence. Considering the influence of boundary layer, the inflation is established in the injection between solid and fluid. The boundary conditions are also shown in Fig. 12. The I is the pressure-inlet, the total pressure is set as 0.221715 MPa, the initial pressure is set as 0.2 MPa. II is the pressure-outlet, the pressure is set as 0.2 MPa. III is the symmetric boundary. IV is the coupled boundary, by which the heat between solid and fluid domain is exchanged. V is the adiabatic boundary, where the heat flux is set as 0. Ambient temperature is 20 °C, and the radiation heat transfer is ignored. The initial temperature of solid region is set as 800 °C.

4.3 Summary of numerical details

The pressure-based solver is applied in the simulation of the transient axisymmetric model. The scheme of the
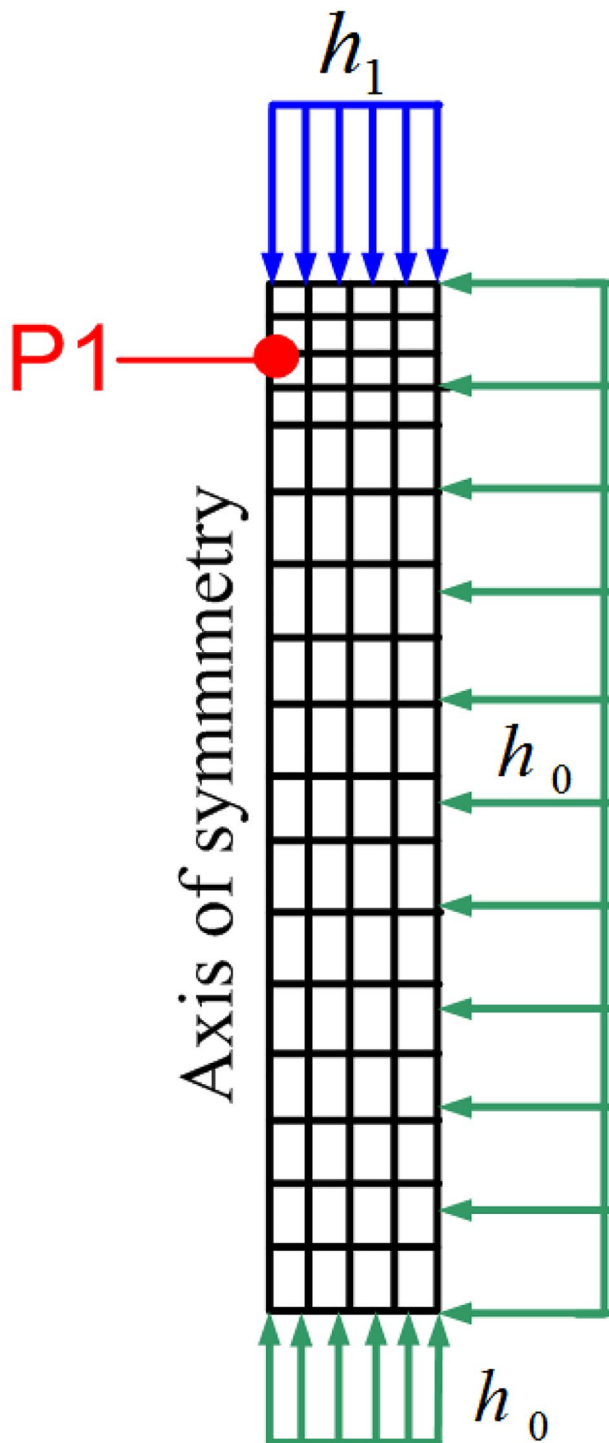
Fig. 9 Finite element model

pressure–velocity coupling analysis is adopted with SIM-PLE algorithm. The transient formulation is based on the first order implicit. In addition, the first order upwind on the

turbulent kinetic energy and specific dissipation rate discretization is chosen, and a second order upwind is selected for the density. Momentum, energy and pressure discretization are based on the second order scheme, the pressure gradient is based on the least squares cell scheme. The value of 1×10^{-6} is considered as the convergence criterion for the energy equation, and 1×10^{-3} is for other equations. The temperature is monitored while calculating, and saved once with the time step of 0.2 s.

5 Results discussion

5.1 Grid and time step independence study

The intensity of grid size has a great influence on the computational time and accuracy of simulation. In order to verify that the grid size is independent of the results. Three different grid sizes are considered to solve this problem. When the flow velocity is large and the Reynolds number exceeds 10^4, the boundary layer thickness is about 1% of the jet diameter in the stagnation region [21, 22], that is to say, the boundary layer thickness is about 0.065 mm in the case. So, for the fluid region, the size of grid closed to the wall is set as 0.0001 mm to ensure the accuracy of the simulation, the grid size becomes lager and lager with the increase of the distance from the wall. In the numerical simulation, three types of grid size (grid 1, 2 and 3) are used, the number of the grid along the axial direction is 60, 120 and 150, respectively. For the solid and jet regions, the quadrilateral grid with 0.5×1 mm is used. The temperature on point P1 shown in Fig. 12 is monitored in the simulation. The temperature curves of grid 1, 2 and 3 are shown in Fig. 13. The average temperature difference between grid 2 and grid 3 is approximately 0.104 °C, It is supposed that the influence of grid size on the temperature can be negligible when the grid size is not more than the size of grid 2. However, the calculation time of grid 3 is much more than that of grid 2, so grid 2 is used in the following calculation to reduce the calculation time.

Similarly, verification of time step independence is done to ensure that the time step does not affect the result of temperature. Five time steps (0.01, 0.05, 0.1, 0.2 and 0.5 s) are selected to simulate the cooling process of sample, variation of temperature on the cooling surface of the sample is shown in Fig. 14. It can be seen from Fig. 14 that the time step has a significant influence on the calculation results of the temperature. When the time step is reduced to 0.2 s, the calculated results of temperature will not change significantly if the time step is further reduced, so 0.2 s is confirmed as the time step in the subsequent simulation.

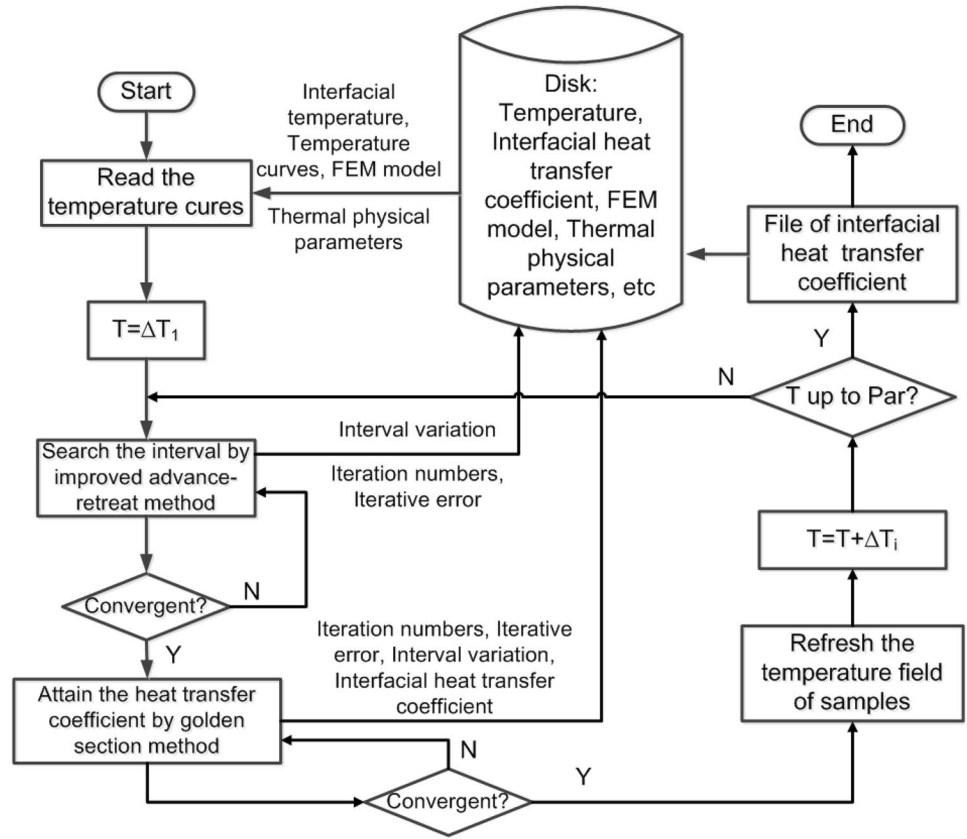**Fig. 10** Flow chart of inverse heat transfer method

Fig. 11 Error between experimental temperature and temperature calculated by inverse heat transfer program
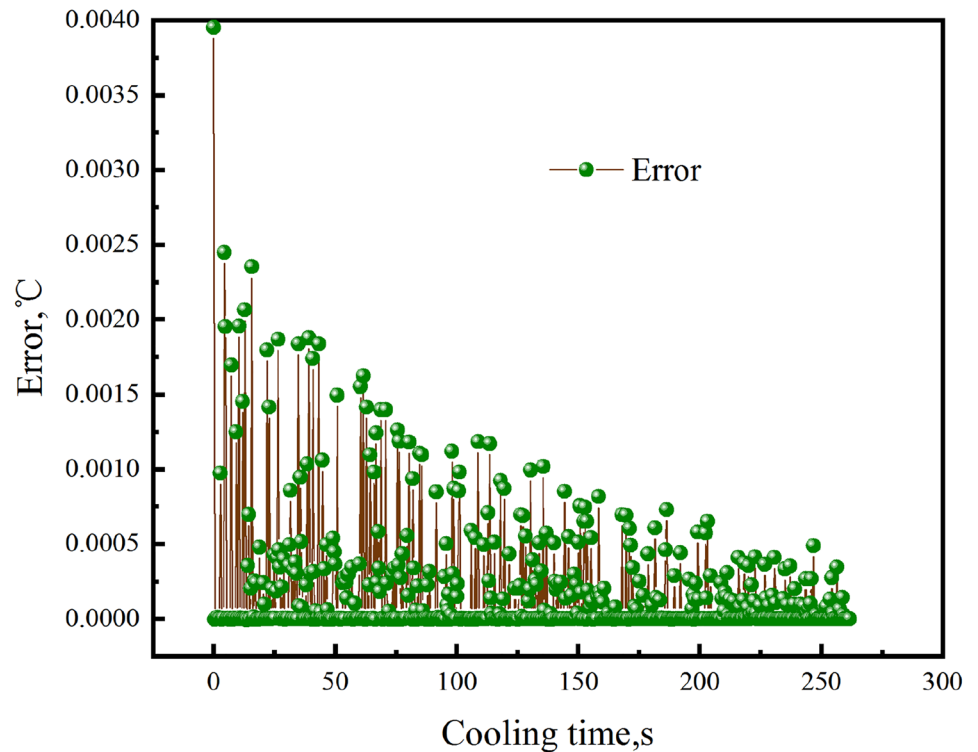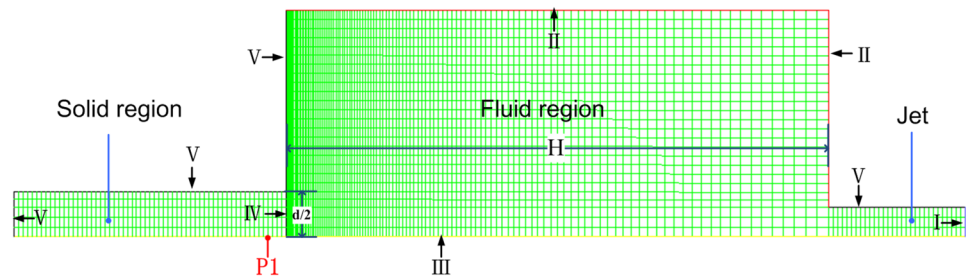
Fig. 12 Geometry model and boundary conditions

5.2 Evaluation of turbulence models capabilities

In the simulation, the turbulence model has a great effect on the flow. In the simulation of air-cooling, the turbulence models widely used are SST k-ω, Realizable k-ε and RNG k-ε. The transport equations of the turbulence models all was controlled by two-equations, which is appropriate for the simulation of air-cooling process. But there are some differences between them.

In the RNG k-ε model, the production of turbulence kinetic energy G_K in the RNG k-ε model is not only related to the flow situation, but also a function of spatial coordinates in the same problem. The RNG k-ε model can better deal with high strain rate and degree of streamline curvature larger flow [22]. The Realizable k-ε model is introduced in the formula of turbulent viscosity content related to the rotation and curvature, it is applied to include the free flow of jet flow and mixed flow. But the Realizable k-ε model for fully developed turbulent flow is valid, the near wall boundary layer of low Reynolds number region will be not appropriate [23]. The SST k-ω model combines the advantages of k-ω model and k-ε model, it is transformed into Wilcox k-ω model near the wall, the standard k-ε model was used for boundary layer and free shear layer [24, 25]. The SST k-ω model near the wall has higher precision, algorithm stability is good, can better simulate flow field effect, the simulation of stagnation point is very good [26, 27].

In order to verify the accuracy of turbulence models, the experiment is done to attain the temperature curve of point P1 shown in Fig. 1 in the air-cooling process. In the experiment, air pressure is 0.2 MPa, the jet distance is 60 mm, the diameter of jet is 6.5 mm, the size of 304 stainless steel sample is $\varnothing 10 \times 30$ mm. The sample is heated to 800 °C, and then cooled. The schematic diagram of experiment is shown in Figs. 2 and 3. The temperature curve of point P1 attained in the experiment is shown in Fig. 15. The air-cooling

Fig. 13 Variation of temperature with cooling time for the different grid size
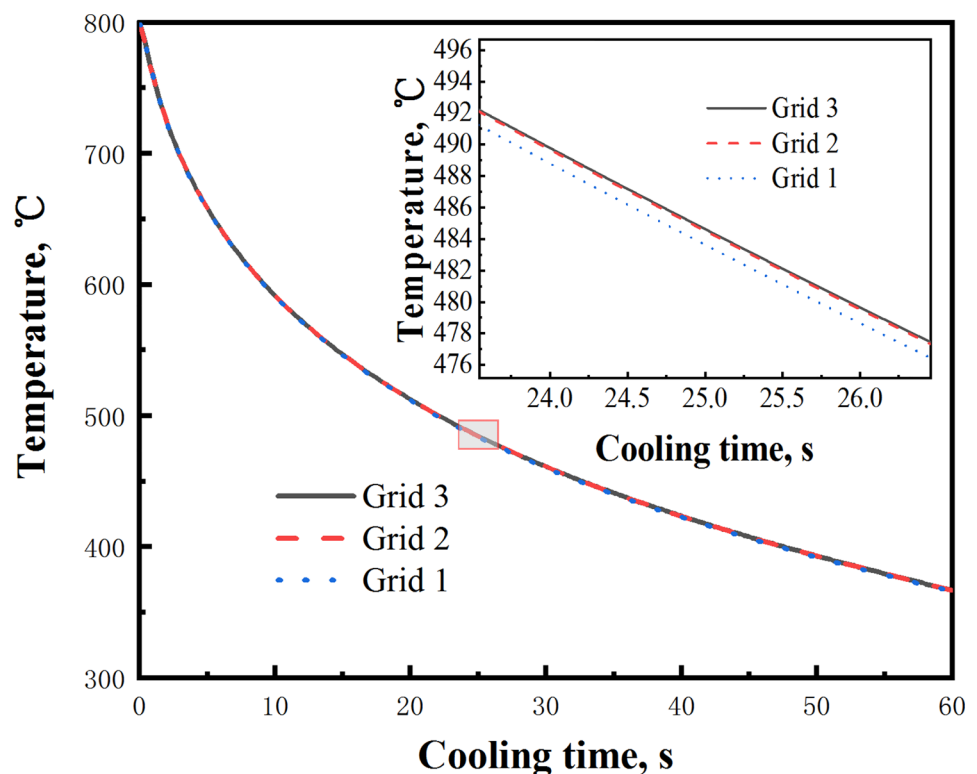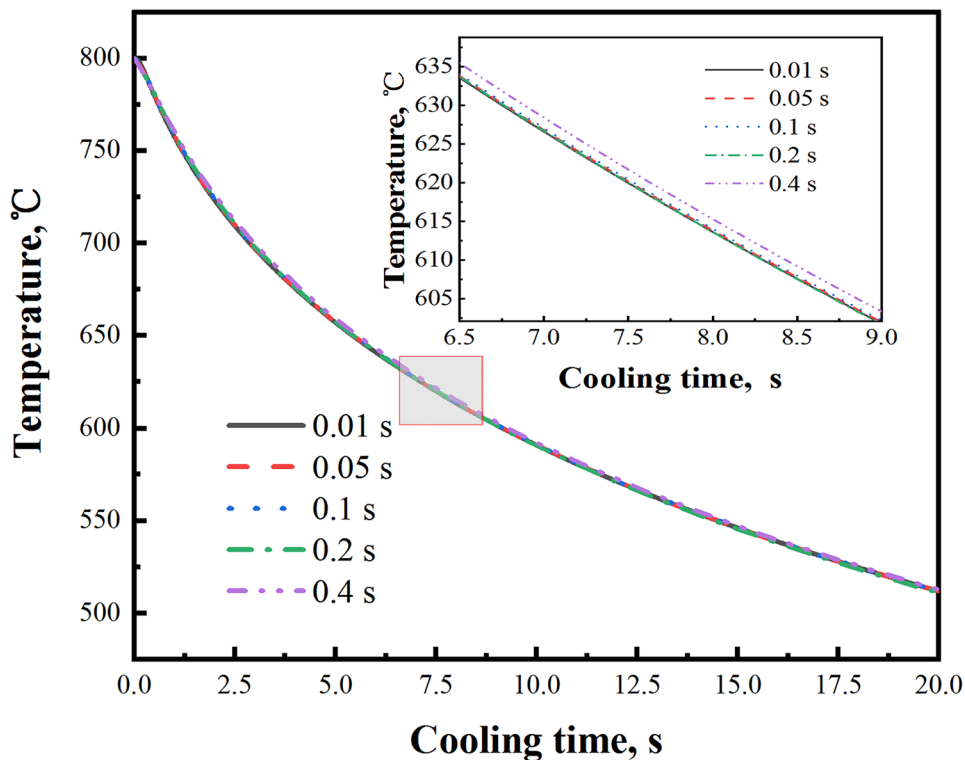
Fig. 14 Variation of temperature with cooling time for the different time steps

process of sample is simulated using SST k-ω, realizable k-ε and RNG k-ε models, respectively. Geometry model and boundary conditions used in the simulation are shown in Fig. 12. The temperature curves of point P1 attained in the simulation are shown in Fig. 15. The temperature curves in Fig. 14 show that the temperatures attained in the simulation by SST k-ω model are more consistent with that attained in the experiment, and the SST k-ω model is more feasible to simulate the air-cooling process.

5.3 Effect of sample diameter on the temperature field

As one of the most important factors affecting the cooling process of samples, the pattern of flow has a significant influence on the cooling rate of samples. The flow pattern of air-cooling is similar to that of impinging jet, and can be subdivided into three characteristic regions: the free jet region, the stagnation region and the wall jet region, as shown in Fig. 16. Due to an intensive exchange of momentum with the surrounding free gas, the flow from the jet spreads radically in the free jet region with a high intermediate flow velocity and a low peripheral flow velocity. When the flow impinges the wall, the flow deflects towards the radical direction, which affects a transition for a wall jet region further downstream. Because of the viscosity of the fluid, the flow velocity decreases sharply inside the cooling surface, and the flow forms a thin boundary layer

which have the flow velocity gradient perpendicular to the cooling surface. The flow rate in the boundary layer is approximately one percent of the free jet region. Before the free jet region transforms into the wall jet region, there is a stagnation region directly underneath the center of the jet, which has a slow flow velocity and a particularly high local heat transfer coefficient [28].

The fluid flow in the stagnation zone has two flow states: laminar flow and wall turbulence. In addition to laminar flow in the main flow direction, the fluid also have an irregular turbulence, which promotes the additional momentum and heat exchange between the different temperature layers.

The additional momentum exchange (additional shear stress) formula [28] between the different flow layers can be obtained

$$\tau = \tau_l + \tau_T = \rho(\nu + \varepsilon_m)\frac{\partial u}{\partial z} \tag{10}$$

where, τ is the total shear stress, τ_l is the shear stress due to the laminar flow, τ_T is the shear stress due to the wall turbulence, ρ is density, ν is the kinematic viscosity, ε_m is the turbulent momentum diffusivity, μ is flow velocity. z is the direction in cylindrical coordinate system.

By using the analogy theory [28], the additional heat exchange formula between the different temperature layers can be obtained according to Eq. (10)

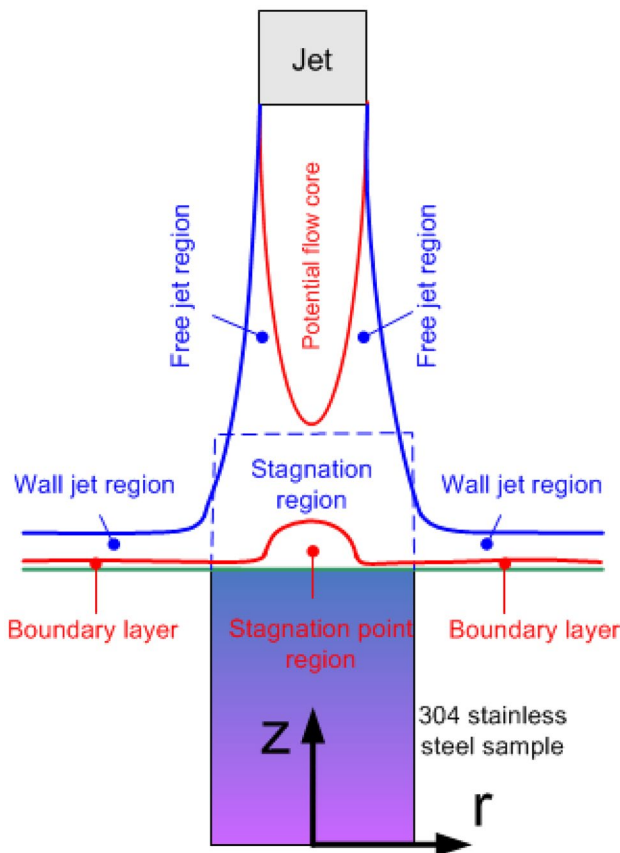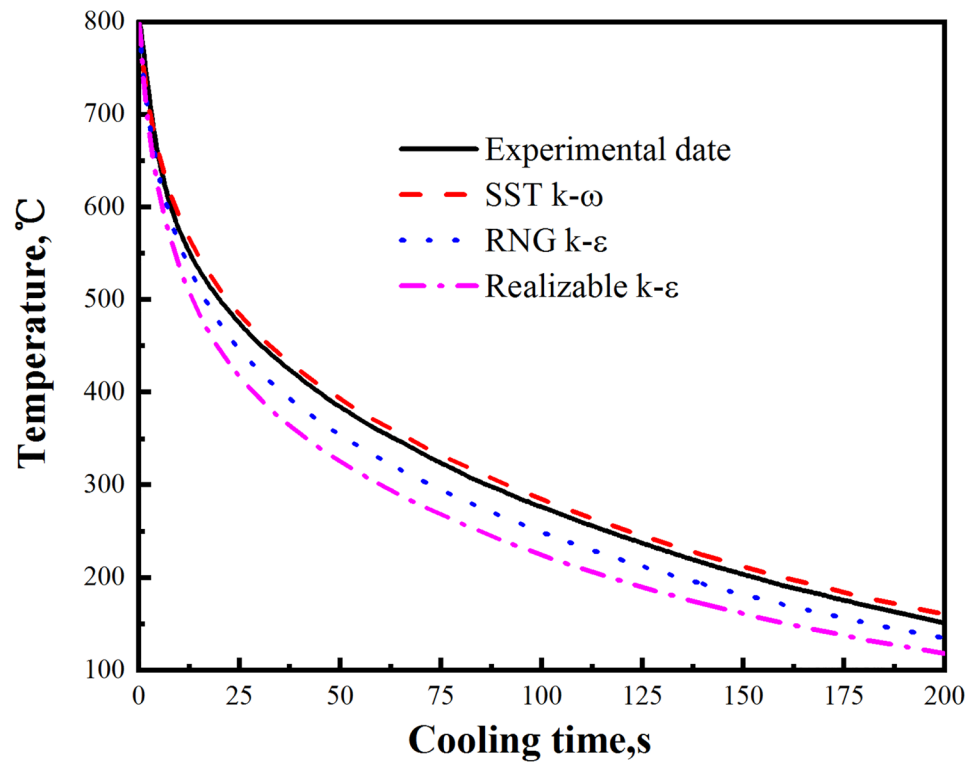**Fig. 15** Temperature curves attained in the simulation and experiment

Fig. 16 Flow regions for air-cooling

$$q = q_l + q_T = -\rho c_p(\alpha + \varepsilon_T)\frac{\partial T}{\partial r} \qquad (11)$$

where, q_l is the heat flux in the laminar flow region. q_T is the heat flux contributed by the wall turbulence. α is the laminar thermal diffusivity. ε_T is the turbulent thermal diffusivity, which is related to the turbulence intensity of wall turbulence. T is temperature. r is the direction in cylindrical coordinate system.

According to Eqs. (10) and (11), the momentum and heat exchange capacity of the stagnation region are much stronger because the additional heat transfer between laminar flow and turbulence flow. And according to Refs [25] and [26], heat transfer in the stagnation region is higher than that in the boundary region, because the Nussel number of the stagnation region is larger than the boundary region.

When cooling time is 60 s, the temperature and flow fields of the samples with the diameter of 10 mm, 20 mm and 30 mm are shown in Fig. 17. The flow velocity in the inlet is about 130 m/s, which is same as the flow velocity in the experiment in Chapter 2.2. The radial temperature distribution at the Sect. 2 mm away from the cooling surface of the sample is shown in Fig. 18. Due to the existence of the stagnation zone and the boundary layer, the radial temperatures of samples with the different diameters have a significant difference. The cooling surface of the sample with the diameter of 10 mm only contacts the stagnation area, and the radial temperature of the sample
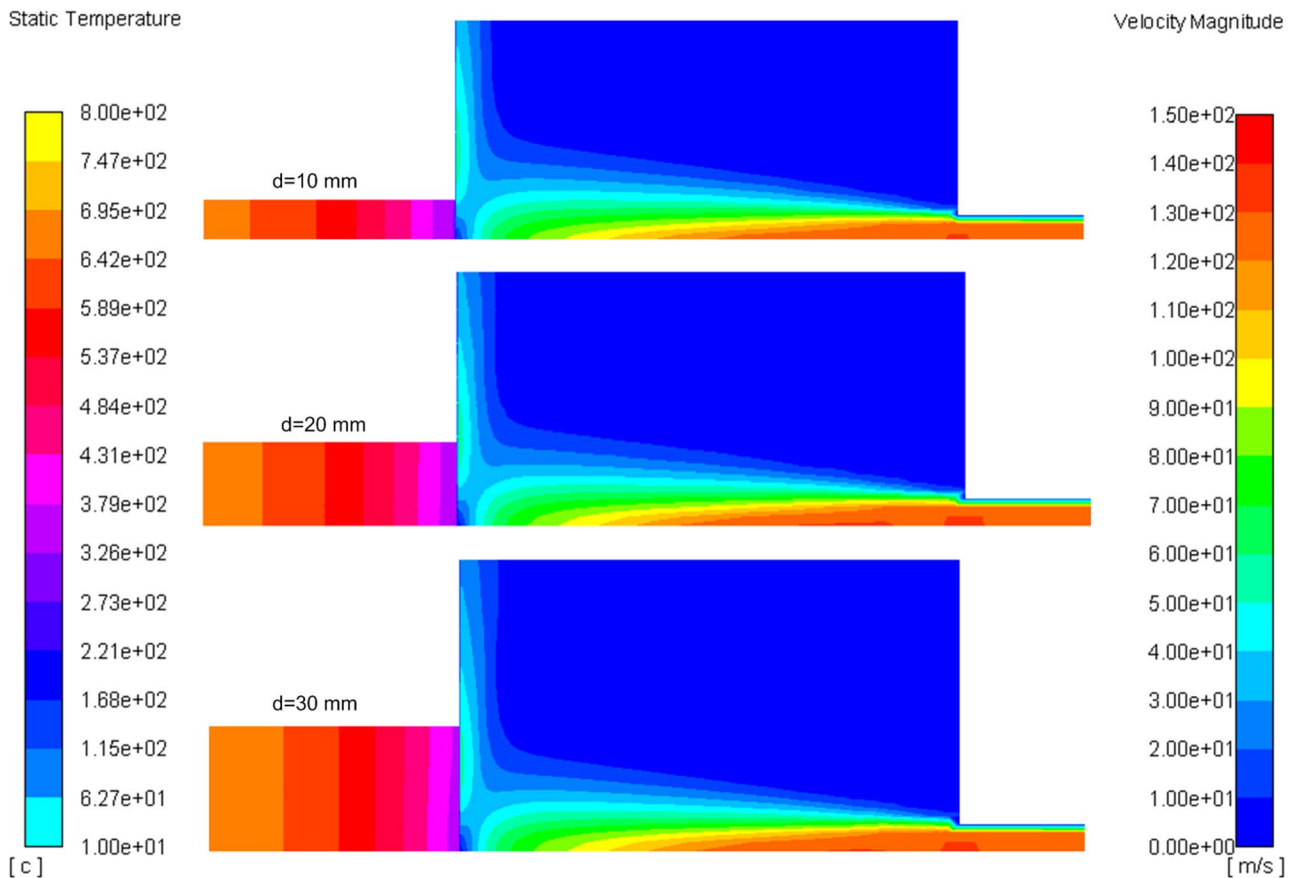
Fig. 17 Temperature field and velocity field of samples with the different diameters

is basically uniform as shown in Fig. 19. With the increase of the sample diameter (d = 20 mm and 30 mm), as shown in Fig. 17, the cooling surface of the sample contacts both the stagnation region and the boundary layer. Compared with the heat exchange rate in the stagnation region, the heat exchange rate in the boundary layer is slower, resulting in the non-uniform cooling in the near-surface temperature of the sample with the diameters of 20 mm and 30 mm, as shown in Fig. 18. Samples with a large diameter (d = 20 mm and 30 mm) show a regularity of low central temperature and high edge temperature in the radial direction. Therefore, when cooling the larger diameter of samples (d = 20 mm and 30 mm), the heat exchange of the samples does not be assumed to the one-dimensional heat exchange.

Figure 19 shows the temperature distribution along the radial direction of the sample at the different sections after cooling for 60 s. Figure 19 show that the temperature value of the same section has no obvious difference. Using the boundary conditions shown in Fig. 12, the air-cooling process of the sample with the diameter of 10 mm can be regarded as the one-dimensional heat transfer.

5.4 Effect of jet distance on the temperature

In order to know the effect of jet distance on the temperature, the jet distances of 30 mm, 60 mm and 90 mm are used in
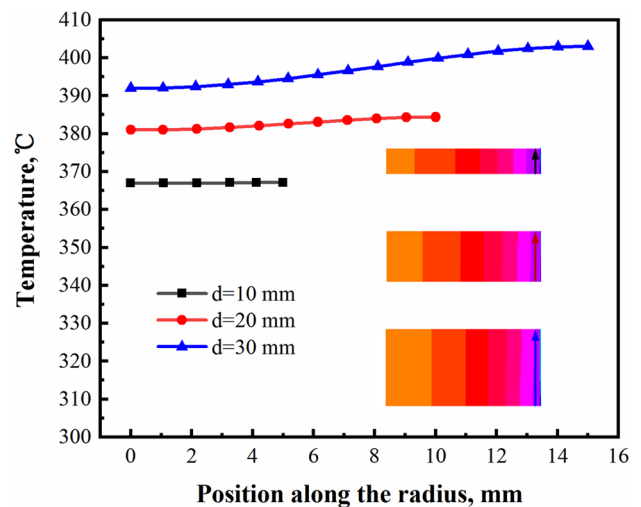

Fig. 18 Radial temperature at Sect. 2 mm away from the cooling surface of samples with the different diameters
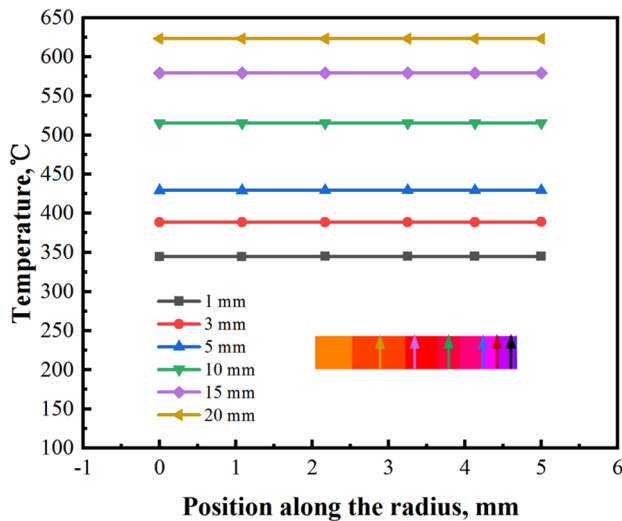
Fig. 19 Radial temperature variations at the sections with the different distances from the cooling surface of sample

Fig. 20 Temperature curves attained in the simulation and experiment

the experiment. Other parameters are same as that in Chapter 4.2. The temperature curves of point P1 attained in the experiment are shown in Fig. 20. The air-cooling process of sample is simulated using SST *k-ω* model, geometry model and boundary conditions used in the simulation is shown in Fig. 12. The temperature curves of point P1 attained in the simulation are shown in Fig. 20. The temperature curves in Fig. 20 show that, for the different jet distance, the temperatures attained in the simulation by SST *k-ω* model are consistent with that attained in the experiment. The SST *k-ω* model for the different jet distances of air cooling has a good simulation precision.

According to the temperature curves attained in the simulation and experiment, the IHTCs can be calculated by the inverse heat transfer method shown in Fig. 10 and the FEM model shown in Fig. 9. The IHTC varied with surface temperature are shown in Fig. 21. The variations and tendency of IHTC with the cooling time agree with the results in in Refs [9] and [19], as shown in Fig. 21. And the IHTCs varied with cooling time are shown in Fig. 22. In experiment, the IHTC at the beginning time rise rapidly because that the gas flow takes time to reach a steady state. For the different jet distance *H*, when the flow begins impinging, IHTC rapidly increases, finally obtaining its maximum and remaining constant. The Nusselt number varied with cooling time are shown in Fig. 23. The variations and tendency of Nusselt number with the cooling time agree with the results in Refs [4] and [26]. But, there is a difference in the value of Nusselt number, and the cooling times of the Nusselt number from the beginning to the steady state is different. The reason is that, the nondimensional jet distance, the flow thermal properties and sample used in the paper are different from those used in Refs [4] and [26].
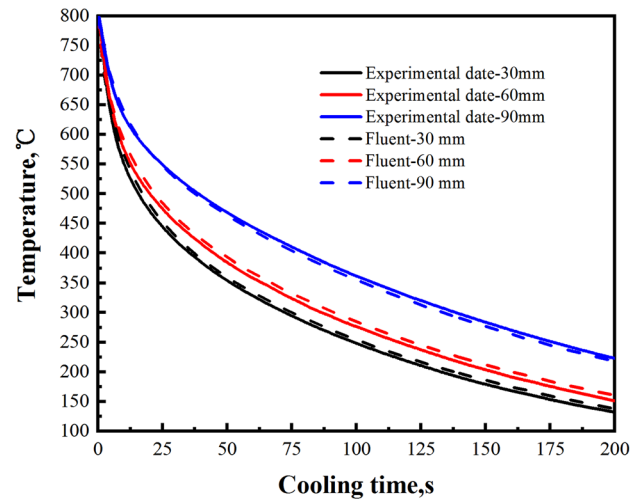
As the jet distance is 30 mm, 60 mm and 90 mm, the IHTCs calculated according to the temperatures attained in the simulation are well consistent with that according to the temperatures attained in the experiment. It confirms that the model, boundary conditions, grid size and time step are more reasonable. Therefore, the temperature curves of different pressure and jet distance can be attained by the CFD numerical simulation based on the Fluent software, then the IHTCs under the different pressure and jet distance can be calculated using the inverse heat transfer method according to the temperature curves under the different conditions.

5.5 IHTCs under the different parameters

Based on the above validated FEM model and boundary conditions, the air-cooling quenching processes with the gas flow rate of 30–130 m/s and the jet distance of 30–90 mm are simulated by using the turbulence model SST *k-ω* based on Fluent software, and the temperature curves on the point P1 shown in Fig. 1 are attained at a time step of 0.2 s in the simulation. According to the temperature curves obtained in the simulation, the IHTCs under the different air-cooling parameters are calculated by the inverse heat transfer method shown in Fig. 10. The IHTCs under the different air-cooing parameters are shown in Fig. 24. The flow velocity near the cooling surface increase with the decrease of jet distance. In addition, the laminar thermal diffusivity *α* and the turbulent thermal diffusivity *ε_t* in Eq. (11) will rise with the increase of the flow velocity near the cooling surface. According to Eq. (11), the larger flow velocity promotes the heat transfer between the flow and sample, and the heat transfer between the flow and sample is much stronger. So, at the same inlet flow velocity, the smaller the jet distance is, the greater the
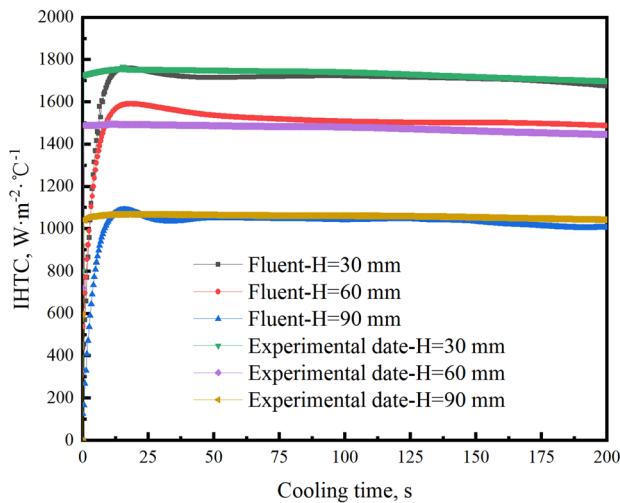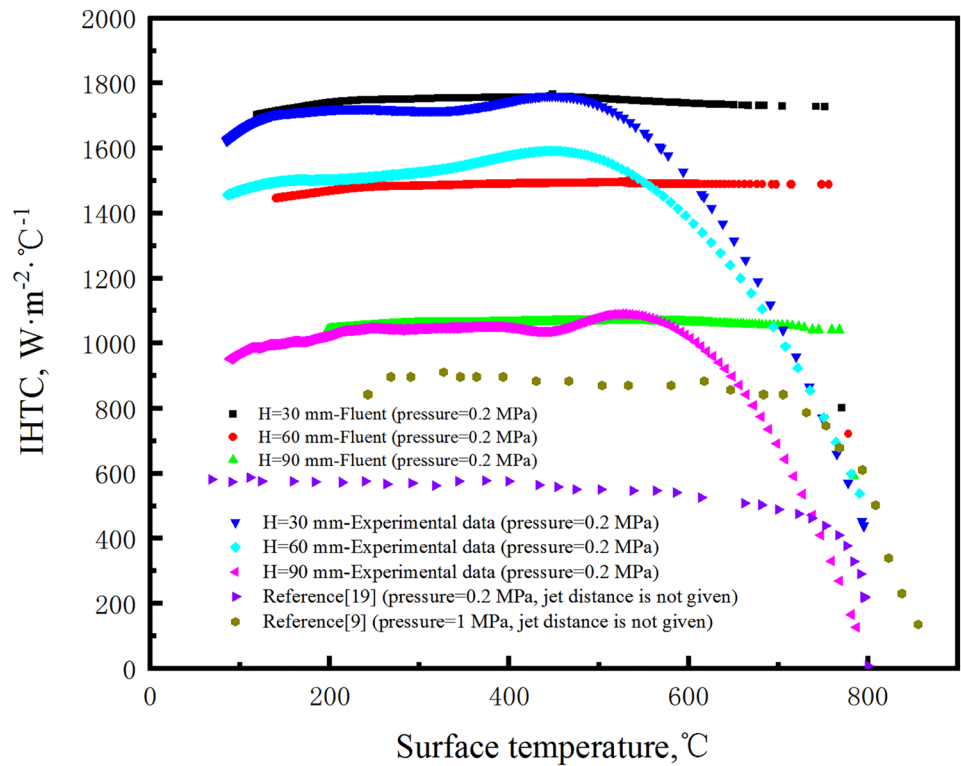
Fig. 21 IHTCs varied with surface temperature
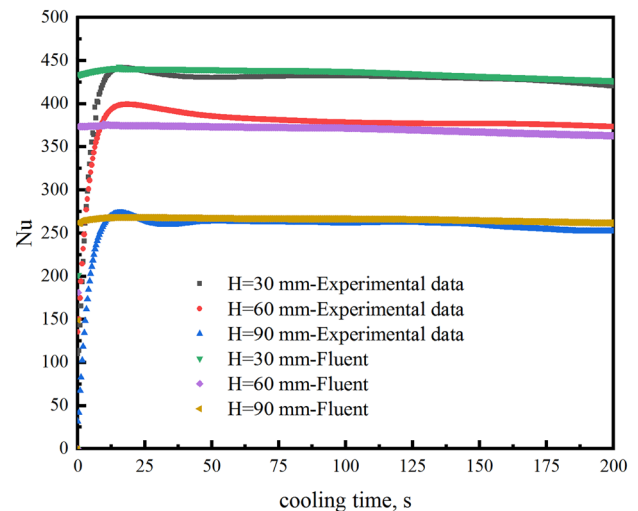


Fig. 22 IHTCs varied with cooling time

Fig. 23 Nu varied with cooling time

IHTC is. And at the same jet distance, the bigger the inlet flow velocity is, the greater the IHTC is.

For the complex heat transfer process, such as the quenching process, metal hot forming and so on, the temperature of cooled part is often simulated by using the IHTC as the third boundary condition [5–10]. By this means, the IHTCs shown in Fig. 24 can be used to accurately calculate the temperature fields of parts with complex shape in the air-cooling process. Moreover, the complex CFD model and multi-physics coupling analysis can be avoided in the numerical simulation.

Fig. 24 IHTCs under the different air-cooling parameter
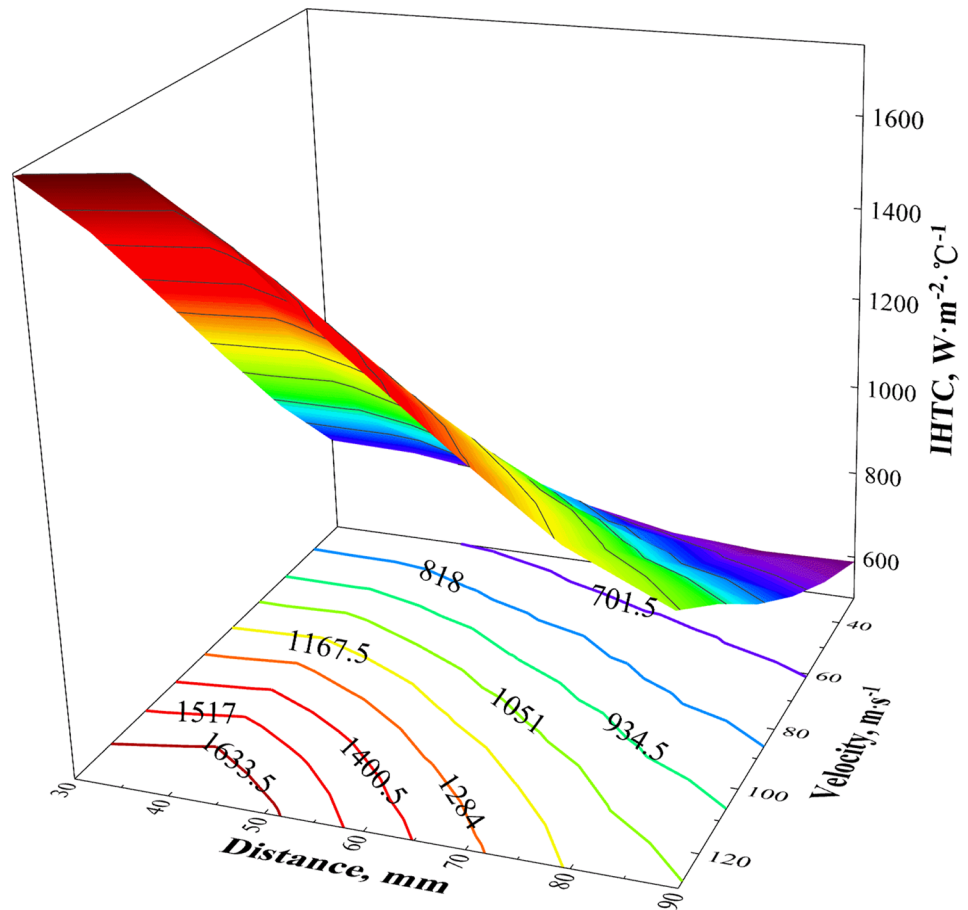
6 Conclusions

Axisymmetric heat transfer model of fluid-thermal-solid coupling is established, and SST k-ω turbulence model is used in the simulation. The results show that, the monitored temperature curve is basically consistent with that of experiment, and the IHTCs calculated by self-developed inverse heat transfer analysis software are also basically consistent.

The influence of the cooling surface diameter of sample on the temperature field is studied. It shows that, the cooling surface temperatures are greatly affected by the flow pattern. Because of the existence of stagnation zone and the wall jet region on the interface, the temperature difference along the radical direction can not be ignored. When the sample with 10 mm diameter, the temperature is uniform along the radical direction. Therefore, the sample with 10 mm diameter is suitable for the study of one-dimensional heat transfer.

The influence of the jet distance on the IHTCs is studied. The results of experiment and simulation are in good agreement. The IHTCs and efficiency of heat transfer are gradually decreased with the increasing of the jet distance. From the velocity fields, the farther the jet distance is, the smaller the flow velocity on the cooling surface, and the heat transfer is slower.

Based on the validated model, the IHTCs at different flow rates and cooling distances are calculated to provide data for the sample with complex shape to simulate the temperature field.

Declarations

Conflict of interest The authors declare that they have no known competing financial interests or personal relationships that could have appeared to influence the work reported in this paper.

References

1. Xu R, Li LX, Yao ZQ (2017) Numerical simulation and experimental verification of extrusion online quenching process of aluminum profile used for traffic. J Cent South Univ T 12:3263–3270. https://doi.org/10.11817/j.issn.1672−7207.2017.12.017

2. Fu P, Zhou P, Zhao TY, Song YP, Huang ZW (2020) Study of the heat transfer coefficient of a nickel-based superalloy in the end-quench test with air. Int J Therm Sci 155:106416. https://doi.org/10.1016/j.ijthermalsci.2020.106416

3. Kang H, Wu D, Zhao XM (2013) Surface Temperature Change of U75V 60 kg/m Heavy Rail During Heat Treatment. J Iron Steel Res Int 20(33–37):67. https://doi.org/10.1016/S1006-706x(13)60053-9

4. Guo Q, Wen Z, Dou RF (2017) Experimental and numerical study on the transient heat-transfer characteristics of circular air-jet impingement on a flat plate. Int J Heat Mass Tran 104:1177–1188. https://doi.org/10.1016/j.ijheatmasstransfer.2016.09.048

5. Li HP, Zhao GQ, Niu ST, Luan YG (2006) Inverse heat conduction analysis of quenching process using finite-element and optimization method. Finite Elem Anal Des 42:1087–1096. https://doi.org/10.1016/j.finel.2006.04.002

6. Hu P, Ying L, Li Y, Liao Z (2013) Effect of oxide scale on temperature-dependent interfacial heat transfer in hot stamping process. J Mater Process Tech 213:1475–1483. https://doi.org/10.1016/j.jmatprotec.2013.03.010

7. Li HP, He LF, Zhang CZ, Cui HZ (2015) Research on the effect of boundary pressure on the boundary heat transfer coefficients between hot stamping die and boron steel. Int J Heat Mass Tran 91:401–415. https://doi.org/10.1016/j.ijheatmasstransfer.2015.07.102

8. Wang HM, Yu W, Cai QW (2012) Experimental study of heat transfer coefficient on hot steel plate during water jet impingement cooling. J Mater Process Tech 212:1825–1831. https://doi.org/10.1016/j.jmatprotec.2012.04.008

9. Cheng H, Xie J, Li J (2004) Determination of surface heat-transfer coefficients of steel cylinder with phase transformation during gas quenching with high pressures. Comp Mater Sci 29:453–458. https://doi.org/10.1016/j.commatsci.2003.11.003

10. Luo X, Yang Z (2017) A new approach for estimation of total heat exchange factor in reheating furnace by solving an inverse heat conduction problem. Int J Heat Mass Tran 112:1062–1071. https://doi.org/10.1016/j.ijheatmasstransfer.2017.05.009

11. Liu XC, Ji K, El Fakir O, Fang HM, Gharbi MM, Wang LL (2017) Determination of the interfacial heat transfer coefficient for a hot aluminium stamping process. J Mater Process Tech 247:158–170. https://doi.org/10.1016/j.jmatprotec.2017.04.005

12. Ilkhchy AF, Jabbari M, Davami P (2012) Effect of pressure on heat transfer coefficient at the metal/mold interface of A356 aluminum alloy. Int Commun Heat Mass 39:705–712. https://doi.org/10.1016/j.icheatmasstransfer.2012.04.001

13. Taler J, Zima W (1999) Solution of inverse heat conduction problems using control volume approach. Int J Heat Mass Tran 42:1123–1140. https://doi.org/10.1016/s0017-9310(98)00280-4

14. Li HP, He LF, Zhang CZ, Cui HZ (2015) Solution of boundary heat transfer coefficients between hot stamping die and cooling water based on FEM and optimization method. Heat Mass Transfer 52:805–817. https://doi.org/10.1007/s00231-015-1602-7

15. Yang JT, Chen W, Li GF, Shi JH (2012) Numerical Simulation of Quenching Air Cooling Process for Steel Rail Based on Fluent. Hot Working Tech 41:165–167. https://doi.org/10.14158/j.cnki.1001-3814.2012.04.04616

16. Yang J, Zhang Y, Gao MX, Fu LH, Song H (2019) Numerical study of transient conjugate heat transfer of the cryo-supersonic air-quenching based on a Mach-weighted pressure-based method. Int J Heat Mass Tran 134:586–599. https://doi.org/10.1016/j.ijheatmasstransfer.2019.01.064

17. Xu ZZ, Liu XJ, Kim HK, Shin JH, Lyu SK (2011) Thermal error forecast and performance evaluation for an air-cooling ball screw system. Int J Mach Tool Manu 51:605–611. https://doi.org/10.1016/j.ijmachtools.2011.04.001

18. Ding CE, Dou RF, Chen C, Tian DP, Guo Q, Wen Z (2017) Experimental measurement of air jet impinging heat transfer coefficient based on 2D transient inverse heat conduction method. Energy Metall Ind 36:28–33. https://doi.org/10.3969/j.issn.1001-1617.2017.01.007

19. Wang XW, Li HP, He LF, Li ZC, Wang ZZ (2019) Estimated temperature-dependent interfacial heat transfer coefficient during gas cooling based on firefly algorithm and finite element method. Heat Mass Transfer 55:2545–2558. https://doi.org/10.1007/s00231-019-02608-y

20. Dou RF, Wen Z, Zhou G (2015) Heat transfer characteristics of water spray impinging on high temperature stainless steel plate with finite thickness. Int J Heat Mass Tran 90:376–387. https://doi.org/10.1016/j.ijheatmasstransfer.2015.06.079

21. Martin H (1977) Heat and mass transfer between impinging gas jets and solid surfaces. Adv Heat Tran Elsevier 13:1–60. https://doi.org/10.1016/S0065-2717(08)70221-1

22. Zargarabadi MR, Rezaei E, Yousefi-Lafouraki B (2018) Numerical analysis of turbulent flow and heat transfer of sinusoidal pulsed jet impinging on an asymmetrical concave surface. Appl Therm Eng 128:578–585. https://doi.org/10.1016/j.applthermaleng.2017.09.059

23. Liu X, Yue S, Lu L, Gao W, Li J (2018) Numerical Simulations of a Gas–Solid Two-Phase Impinging Stream Reactor with Dynamic Inlet Flow. Energies 11:1913. https://doi.org/10.3390/en11071913

24. Illyas SM, Bapu BRR, Rao VVS (2018) Heat transfer and flow visualization of swirling impinging jet on flat surface using helicoid inserts. J Visual-Japan 21:729–749. https://doi.org/10.1007/s12650-018-0493-3

25. Bazdidi-Tehrani F, Karami M, Jahromi M (2011) Unsteady flow and heat transfer analysis of an impinging synthetic jet. Heat Mass Tran 47:1363–1373. https://doi.org/10.1007/s00231-011-0801-0

26. Yu PP, Zhu KQ, Shi Q, Yuan NY, Ding JN (2017) Transient heat transfer characteristics of small jet impingement on high-temperature flat plate. Int J Heat Mass Tran 114:981–991. https://doi.org/10.1016/j.ijheatmasstransfer.2017.06.112

27. Zhu KQ, Yu PP, Yuan NY, Ding JN (2018) Transient heat transfer characteristics of array-jet impingement on high-temperature flat plate at low jet-to-plate distances. Int J Heat Mass Tran 127:413–425. https://doi.org/10.1016/j.ijheatmasstransfer.2018.07.099

28. Yang SM, Tao WQ (2006) Heat Transfer, 3rd edn. Higher Education Press, Beijing